RESEARCH ARTICLE

Coherence Thermodynamics: A Phenomenological Framework and a Numerical Field Model for Black-Hole Morphology

Jordan Barton [1,*]

[1] Independent Researcher, Denver, United States

Abstract

Quantum coherence is increasingly recognised as a thermodynamic resource that free energy alone cannot describe. This work develops a phenomenological thermodynamics for coherence-information (C-I) systems, idealised systems composed only of information and the coherent relations among its elements, and tests a numerical realisation of it against black-hole morphology. A minimum-action postulate, $\Delta C \cdot \Delta I \geq h/\pi$, is combined with a gradient-based semantic entropy and an equipartition-based semantic temperature to formulate five laws and three dimensionally consistent operating modes. For black holes the framework gives a thermodynamic coherence $C_T = 2/(Mc^2)$, which grows as the hole loses mass. A three-dimensional field model encodes U(1), $\mathbb{Z}_2$ and $\mathbb{Z}_3$ symmetry breaking through the geometric phase $m\theta + \omega R + \lambda_{\text{vert}} \cos\phi$ and was examined with grid-convergence tests, control runs with azimuthal orders $m = 1$-6 and closed-form predictions. The azimuthal phase contains a phase-defect line on the symmetry axis. Without regularisation, the maximum field gradient scales inversely with the grid spacing and the axial enhancement of the certainty ratio grows with resolution. With a core radius $a \geq 0.5$, all diagnostics converge to within 3%. The number of decoherence maxima is always $2m$, so the six hot-spot-like features follow directly from the choice $m = 3$. Their spiral pitch, $-\omega/m$, and hemispheric twist, $-2\lambda_{\text{vert}} \cos\phi/m$, agree with the simulations to within 9% and 0.3%, respectively. The model therefore maps imposed symmetry parameters onto observable morphology through explicit relations, yielding falsifiable predictions such as a flux quasi-periodicity at $2m$ times the hot-spot orbital frequency, while its astrophysical interpretation remains phenomenological.

Keywords: quantum coherence, information thermodynamics, black-hole jets, phase singularity, numerical convergence.

1 Introduction

Information is physical: erasing a bit costs at least $k_B T \ln 2$ of heat [1], and quantum coherence can act as a thermodynamic resource. A small, phase-controlled

Submitted: 20 April 2026
Revised: 29 May 2026
Accepted: 01 July 2026
Published: 11 November 2026

Vol. 3, **No.** 1, 2027.
10.62762/JNSPM.2026.976035

***Corresponding author:**
✉ Jordan Barton
jbiophysics@gmail.com

Citation
Barton, J. (2026). Coherence Thermodynamics: A Phenomenological Framework and a Numerical Field Model for Black-Hole Morphology. *Journal of Numerical Simulations in Physics and Mathematics*, 3(1), 60–72.

© 2026 by the Authors. Published by Institute of Central Computation and Knowledge. This is an open access article under the CC BY license (https://creativecommons.org/licenses/by/4.0/).

atomic coherence lets a heat engine extract work from a single bath without violating the second law [2], and noise-induced coherence can raise the power of laser and photocell engines [3]. Resource-theoretic studies show that coherence must be quantified separately from energy and entropy [4]: coherence imposes constraints on state transformations that free energy does not capture [5], Gibbs-preserving maps can create coherence that thermal operations cannot [6], some of these maps carry an unbounded coherence cost [7], and coherence is particularly valuable at low temperature [8]. Geometry alone can also reshape spectra enough to drive thermodynamic transitions, as shown for shape-controlled Bose gases [9] and geometry-induced asymmetric level coupling [10].

These results suggest a broader question that motivates the present work: what thermodynamic description applies to a system made only of information and the coherent relations among its elements? Such coherence-information (C-I) systems are idealisations, in the spirit of Wheeler's "it from bit" [11] and Schrödinger's picture of order sustained by exporting entropy [12]. A C-I system that becomes more ordered internally must produce entropy in its surroundings, so its thermal profile is inverted relative to a heat engine: a cold, ordered interior and a hot exterior (Table 1). Figure 1 sketches the corresponding reaction path: contradictory input raises the semantic free energy to an excited state, and its resolution lowers it below the starting value, with the difference accommodated via non-local reconfiguration outside the C-I system itself. Black holes are a natural test case, because their thermodynamics is fixed by a few parameters [13, 14] and their surroundings show rich, well-observed structure.

Earlier versions of this framework reported black-hole-like features in a numerical field model but did not test whether those features were numerically converged or simply inherited from the chosen input geometry. This paper addresses that gap. Its contributions are:

1. a phenomenological framework–postulates, semantic entropy and temperature, five laws and three operating modes–with all quantities stated in SI units (Section 2);
2. the black-hole relation $C_T = 2/(Mc^2)$ (Section 3);
3. a convergence analysis that identifies a phase-defect line in the model and a regularisation that removes it (Sections 4-5.1);

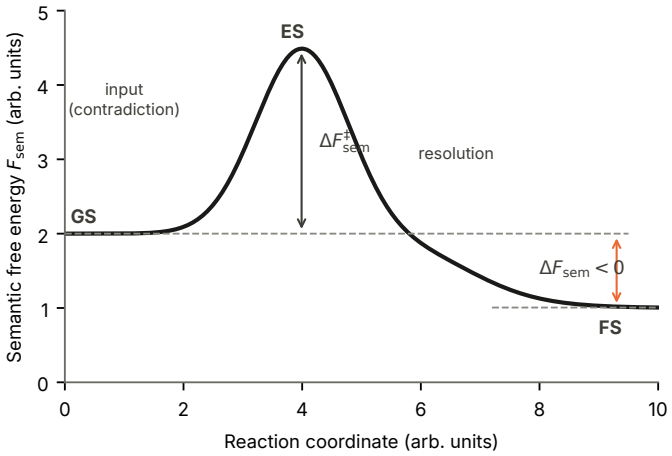


Figure 1. Schematic reaction path of contradiction resolution in a C-I system. Contradictory input lifts the semantic free energy $F_{\rm sem}$ from the ground state (GS) over a barrier $\Delta F^{\ddagger}_{\rm sem}$ at the excited state (ES); resolution leads to a more ordered final state (FS) with $\Delta F_{\rm sem} < 0$, so that at least $-\Delta F_{\rm sem}/T^*$ of entropy is accommodated via non-local reconfiguration outside the C-I system itself. Units are arbitrary.

4. control experiments and closed-form relations linking the symmetry parameters m, ω and $\lambda_{\rm vert}$ to hot-spot multiplicity, spiral pitch and hemispheric twist, from which falsifiable predictions follow (Sections 5.3-6).

Table 1. Thermal profile of a Carnot engine and of a C-I system.

Property	Carnot engine	C-I system
Interior	Hot reservoir	Cold, ordered
Exterior	Cold sink	Hot, disordered
Driving process	Heat flow down a thermal gradient	Contradiction resolution
Output	Mechanical work	Ordered structure

2 Theoretical Framework

2.1 Postulates

The framework rests on two postulates. They are phenomenological: they are not derived from quantum mechanics, and their justification lies in the consequences tested below.

Postulate 1 (certainty bound). Forming a coherent relation requires comparing at least two elements, each carrying at least the quantum of action $\hbar$ [15]. The coherence and information variables of any C-I process

therefore obey

$$\boxed{\Delta C \cdot \Delta I \geq 2\hbar = \frac{h}{\pi}}. \tag{1}$$

The bound has the form of a Heisenberg relation [16], a lower limit on a product of conjugate quantities. Unlike Shannon information [17], which ignores meaning, ΔI here refers to relations that must be actively resolved; the resolution is treated as thermodynamic work. The dimensionless certainty ratio

$$R = \frac{\Delta C \cdot \Delta I}{h/\pi} \tag{2}$$

indicates whether coherent processing is possible ($R \geq 1$) or not ($R < 1$).

Postulate 2 (coherence field). Coherence is relational, and superselection rules (SSRs) forbid some operations when no reference frame is available [18]. I assume a non-depletable coherence field that acts as a shared reference frame: it enables otherwise forbidden transformations without being consumed and couples the C-I system to environmental degrees of freedom in which entropy is produced. The field is characterised by three symmetry-breaking ingredients matching the three SSRs of Gour and Spekkens [18]: a U(1) phase reference (radial twist ω), a $\mathbb{Z}_2$ chirality reference (vertical modulation λ_{vert}) and a partial orientation reference that reduces SO(3) to $\mathbb{Z}_m$ (azimuthal order m; $m = 3$ in the baseline). A threefold harmonic of this kind also appears in the triaxial three-body correlations of atomic nuclei [19]; the analogy is one of symmetry only.

A corollary is the maxim "Existential In, Existential Out" (EIEO): operations without a phase reference cannot create phase coherence from incoherent states [18], so a C-I system can produce coherent output only from input that already carries coherent structure.

2.2 Semantic Entropy

The adjective "semantic" labels quantities defined on C-I systems; all are intended as physical quantities. Let $\sigma(\mathbf{r})$ be the information field. Semantic entropy measures how far its local gradient departs from the root-mean-square (RMS) value G_0:

$$S^*_{\text{sem}} = \alpha\, k_B \ln \frac{1}{C_S}, \qquad C_S = \exp\left[-\left(\frac{|\nabla\sigma|}{G_0}\right)^{3/2}\right], \tag{3}$$

so that $S^*_{\text{sem}} = \alpha k_B (|\nabla\sigma|/G_0)^{3/2}$ exactly. Here $G_0 = \langle|\nabla\sigma|^2\rangle^{1/2}$ is averaged over the domain, and $\alpha \in (0, 1]$ is the coherence scalar, the fraction of activity that contributes to a single resolution trajectory (Eq. (A1)). Table 2 compares S^*_{sem} with the Boltzmann [20], Shannon [17] and von Neumann [21] entropies: all are logarithmic, but S^*_{sem} is built from a field gradient and weighted by α.

Table 2. Entropy definitions compared in this work.

Name	Form
Boltzmann	$S = k_B \ln W$
Shannon	$H = -\sum_i p_i \log p_i$
von Neumann	$S_{\text{vN}} = -\text{Tr}(\rho \ln \rho)$
CT (this work)	$S^*_{\text{sem}} = \alpha\, k_B \ln C_S^{-1}$

2.3 Semantic Temperature

By analogy with Maxwell's kinetic theory [22], where $\frac{1}{2}m\langle v^2\rangle = \frac{3}{2}k_BT$, the phase rate $\partial_0\phi$ of the coherence field $\Psi = e^{i\phi}$ replaces molecular velocity and a semantic kinetic parameter κ_Ψ [J s^2 m^{-3}] replaces mass. Equipartition then gives

$$T^* = \frac{\kappa_\Psi V_\Psi}{N k_B} \langle(\partial_0\phi)^2\rangle, \tag{4}$$

in kelvin, with V_Ψ the semantic volume and N the number of processing elements (units in Appendix A).

2.4 Five Laws

The laws below are stated briefly; derivations are given in Appendix B.

Zeroth law. Systems in mutual semantic equilibrium share the same T^*; semantic heat flows from higher to lower T^* until $T^*_A = T^*_B$.

First law. By analogy with Gibbs' fundamental relation [23, 24],

$$dE_{\text{sem}} = T^* dS^* + \mu\, dN + \Phi\, d\alpha, \tag{5}$$

with semantic heat T^*dS^*, entity work $\mu\, dN$ and coherence work $\Phi\, d\alpha$.

Second law. Entropy obeys the local balance [24, 25]

$$\frac{\partial s}{\partial t} = -\nabla \cdot \mathbf{j}_R + \Pi, \qquad \Pi \geq 0, \tag{6}$$

so local ordering ($\partial s/\partial t < 0$) requires $\nabla \cdot \mathbf{j}_R > \Pi$, i.e. entropy export to the surroundings.

Third law. As $T^* \to 0$, $\alpha \to 1$, $S^* \to S^*_0$ and random phase agitation vanishes, in parallel with the Nernst theorem [26, 27] and Planck's formulation [28].

Fourth law. Following Vopson's mass-energy-information hypothesis [29], which combines Landauer's bound [1] with mass-energy equivalence [30], information of density ρ_I [bit m^{-3}] carries the mass density

$$\rho = \rho_I \frac{k_B T^* \ln 2}{c^2}. \tag{7}$$

2.5 Operating Modes

A C-I system that interacts with its environment needs a resting state, a processing state and an output state. Postulate 1 must hold in each, so each mode pairs a coherence variable with an information variable whose product has units of action (Table 3). In Mode 2 the thermodynamic coherence $\Delta C_T = 1/(T^* S^*)$ is the system's susceptibility to coherence-organising work: the smaller $T^* S^*$, the less energy is needed per unit of reorganisation.

Table 3. Conjugate variables of the three operating modes. In every mode $[\Delta C][\Delta I] = \mathrm{J\,s}$.

Mode	Coherence	Information
1 Standing state	ΔC_S: phase, rad	ΔI_S: action, J s
2 Computation crucible	$\Delta C_T = 1/(T^* S^*)$, J^{-1}	ΔI_T: impulse, J^2 s
3 Holographic interface	ΔC_h: intensity, W m^{-2}	ΔI_h: area×time^2, m^2 s^2

3 Application to Black Holes

With the Bekenstein-Hawking entropy [13, 14], $S = 4\pi G k_B M^2/(\hbar c)$, and the Hawking temperature, $T_H = \hbar c^3/(8\pi G M k_B)$, the product is $T_H S = \frac{1}{2} M c^2$. Hence

$$C_T = \frac{1}{T_H S} = \frac{2}{M c^2}. \tag{8}$$

Thermodynamic coherence grows as a black hole loses mass. To an external observer evaporation increases the entropy of the radiation; in the C-I reading the interior becomes more ordered at the same time, consistent with EIEO and with the inverted profile of Table 1. For Sgr A* ($M \approx 4.3 \times 10^6\, M_\odot$) and M87* ($M \approx 6.5 \times 10^9\, M_\odot$), $T_H \approx 1.4 \times 10^{-14}$ K and 9.5×10^{-18} K, far below $T_{\mathrm{CMB}} \approx 2.7$ K, so both absorb more than they emit.

4 Numerical Model and Methods

4.1 Fields

On a cubic domain $[-L, L]^3$ with spherical coordinates (R, θ, ϕ) and cylindrical radius $\varrho = (x^2 + y^2)^{1/2}$, the information field is

$$\sigma(\mathbf{r}) = g(R)\, f_a(\varrho) \cos \Phi_{\mathrm{geo}},\ \Phi_{\mathrm{geo}} = m\theta + \omega R + \lambda_{\mathrm{vert}} \cos\phi, \tag{9}$$

with Gaussian envelope $g = \exp(-R^2/w^2)$ and axial factor $f_a = [\varrho^2/(\varrho^2 + a^2)]^{m/2}$. The original model corresponds to $a = 0$ ($f_a \equiv 1$); the role of a is explained in Section 4.2. From σ the model computes

$$\Gamma = \frac{|\nabla\sigma|^2}{1 + |\nabla\sigma|^2}\,(1 - g^2), \tag{10}$$

$$T^* = T_0 \left(1 + \beta_T \frac{|\nabla\sigma|}{|\nabla\sigma|_{\max}}\right), \tag{11}$$

$$\mathbf{j}_{\mathrm{sem}} = -k_{\mathrm{sem}} \nabla T^*, \tag{12}$$

$$R = \frac{\Delta C_T\, \Delta I_T}{h/\pi}, \quad \Delta C_T = \frac{1}{T^* S^*}, \tag{13}$$

$$\Delta I_T = \mathcal{I}_0 \left(\frac{|\nabla\sigma|}{|\nabla\sigma|_{\max}}\right)^2,$$

where $\Gamma \in [0, 1)$ is the decoherence field, T_0 is set to the Hawking temperature, S^* follows Eq. (3) with $\alpha = 1$, and $\mathcal{I}_0$ [J^2 s] is an impulse scale. Because $\mathcal{I}_0$ only rescales R, morphological results below use R normalised by its 99.5th percentile, $\hat{R}$. With $\mathcal{I}_0 = 1\,\mathrm{J}^2\,\mathrm{s}$ the original implementation gives $R \sim 10^{47}$-10^{49} everywhere in the domain, so the threshold $R \geq 1$ is satisfied trivially; it becomes informative only once $\mathcal{I}_0$ is fixed independently. Combining the definitions gives $\hat{R} \propto |\nabla\sigma|^{1/2}/T^*$.

4.2 Phase-Defect Line and Its Regularisation

With $a = 0$ the azimuthal phase $m\theta$ is undefined on the z-axis, so σ has a line discontinuity there. Its azimuthal gradient is $|\varrho^{-1}\partial_\theta\sigma| = mg|\sin\Phi_{\mathrm{geo}}|/\varrho$, which diverges as $\varrho \to 0$. On a grid of spacing h the computed maximum is therefore set by the nearest grid point, $|\nabla\sigma|_{\max} \propto 1/h$, and every quantity normalised by $|\nabla\sigma|_{\max}$–T^*, ΔI_T and R–depends on resolution. The axis is a phase dislocation of charge m, of the kind familiar from wave fields [31]. The factor f_a makes the amplitude vanish as ϱ^m on the axis, which removes the divergence while leaving the field essentially unchanged for $\varrho \gg a$. The core radius a is a model parameter; its physical interpretation is discussed in Section 6.2.

4.3 Discretisation, Parameters and Diagnostics

Gradients are computed with second-order central differences (second-order one-sided at the boundaries) [32]. Unless stated otherwise $N = 128$ points per axis, $L = 10$, $w = 15$, $m = 3$, $\beta_T = 0.1$ and $a = 0.5$ (Table 4). Three diagnostics are

used: (i) the ring radius r^* at which the azimuthal mean of Γ in the equatorial plane is largest; (ii) the number of local maxima of Γ (and of $\hat{R}$) on that ring, counted with a prominence threshold of 5% of the profile range; (iii) the azimuth of the maxima, obtained from the phase of the $2m$-th Fourier coefficient of the azimuthal profile. Profiles are sampled with bilinear interpolation at 720-2880 azimuths. The morphology maps of Section 5.2 use a larger box, $L = 20$ with $N = 257$ ($h = 0.156$, so that $a \geq 3h$), and odd N so that the planes $x = 0$, $y = 0$ and $z = 0$ lie exactly on the grid.

Table 4. Model parameters (code units).

Symbol	Baseline	Role
L	10	Half-width of the domain
N	128	Grid points per axis (48-192 in tests)
w	15	Gaussian width (10-20 in tests)
m	3	Azimuthal order, $\mathbb{Z}_m$ (1-6 in tests)
ω	0.1	Radial U(1) twist
λ_{vert}	0.01	Polar $\mathbb{Z}_2$ modulation
a	0.5	Defect-core radius (0-2 in tests)
β_T	0.1	Temperature sensitivity
k_{sem}	3.2×10^{23}	Semantic conductivity (fitted)

5 Results

5.1 Grid Convergence

For $a = 0$ the product $h\,|\nabla\sigma|_{\max}$ stays at 1.08 ± 0.01 for N from 48 to 192 (Figure 2(a)), confirming the $1/h$ scaling, and the RMS gradient G_0 rises slowly from 0.339 to 0.441, the logarithmic growth expected from $\int \varrho^{-2}\,\varrho\,d\varrho$. Quantities that do not involve the axis converge: the mean of Γ changes by 0.6% between $N = 128$ and 192, and $r^* = 4.5$ for $N \geq 128$. The axial contrast of the certainty ratio, defined as the ratio of the median $\hat{R}$ on the axis ($\varrho < 0.6$, $2 < |z| < 8$) to that in the equatorial shell ($3 < \varrho < 7$, $|z| < 1$), does not converge: it rises from 2.71 to 2.95 to 3.26 for $N = 96$, 128 and 192 (Figure 2(b)). Decoherence on the axis behaves the same way, with an axial-to-equatorial ratio of 5-6.

With regularisation the picture changes. For $a = 0.5$, $|\nabla\sigma|_{\max}$ varies by less than 3% between $N = 128$ and 192 and the axial contrast of $\hat{R}$ settles at 1.78 (change 1.7%). For $a = 1$ the contrast is 1.03, and for $a = 2$ the axis is depleted (contrast 0.47). The axial, jet-like enhancement of R is therefore a property of the defect core: it is finite and converged only for $a \gtrsim 3h$, and its strength is set by a.

5.2 Baseline Morphology

Figures 3, 4 and 5 show the regularised model ($a = 0.5$) in the three coordinate planes, without twist and with the baseline twist. In the equatorial plane $\hat{R}$ is largest near the centre and is cut by $2m = 6$ dark spokes, the directions where $\sin\Phi_{\text{geo}} = 0$ and

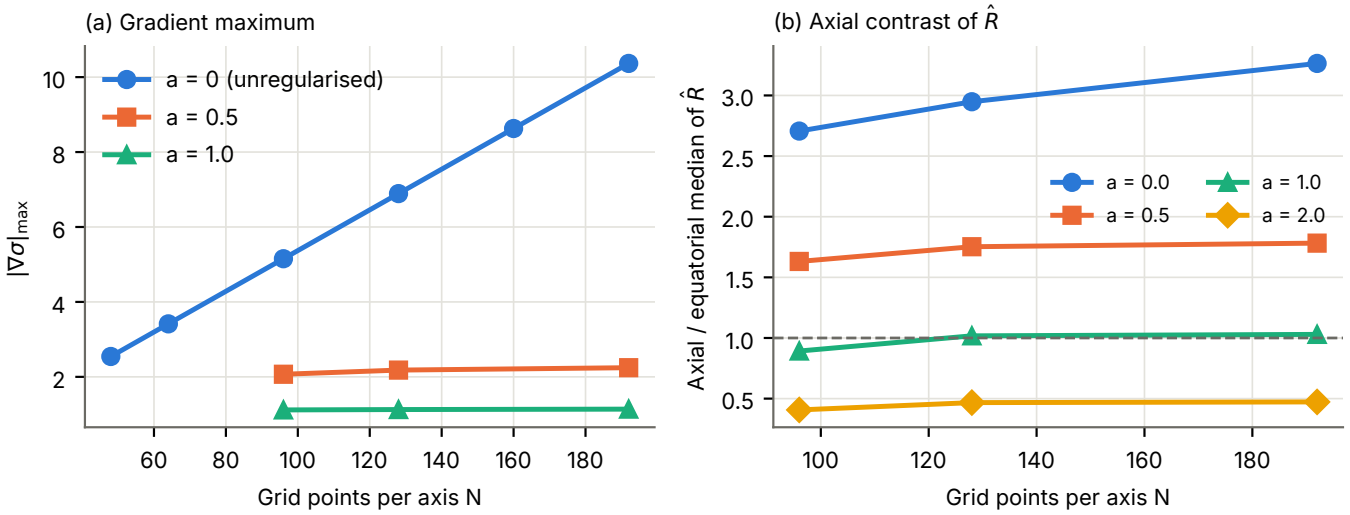


Figure 2. Grid convergence. (a) Maximum gradient magnitude versus grid points per axis N: it grows as $1/h$ without regularisation ($a = 0$) and converges for $a = 0.5$ and 1. (b) Ratio of the median certainty ratio on the symmetry axis to that in the equatorial shell, for four core radii; the dashed line marks equal values.

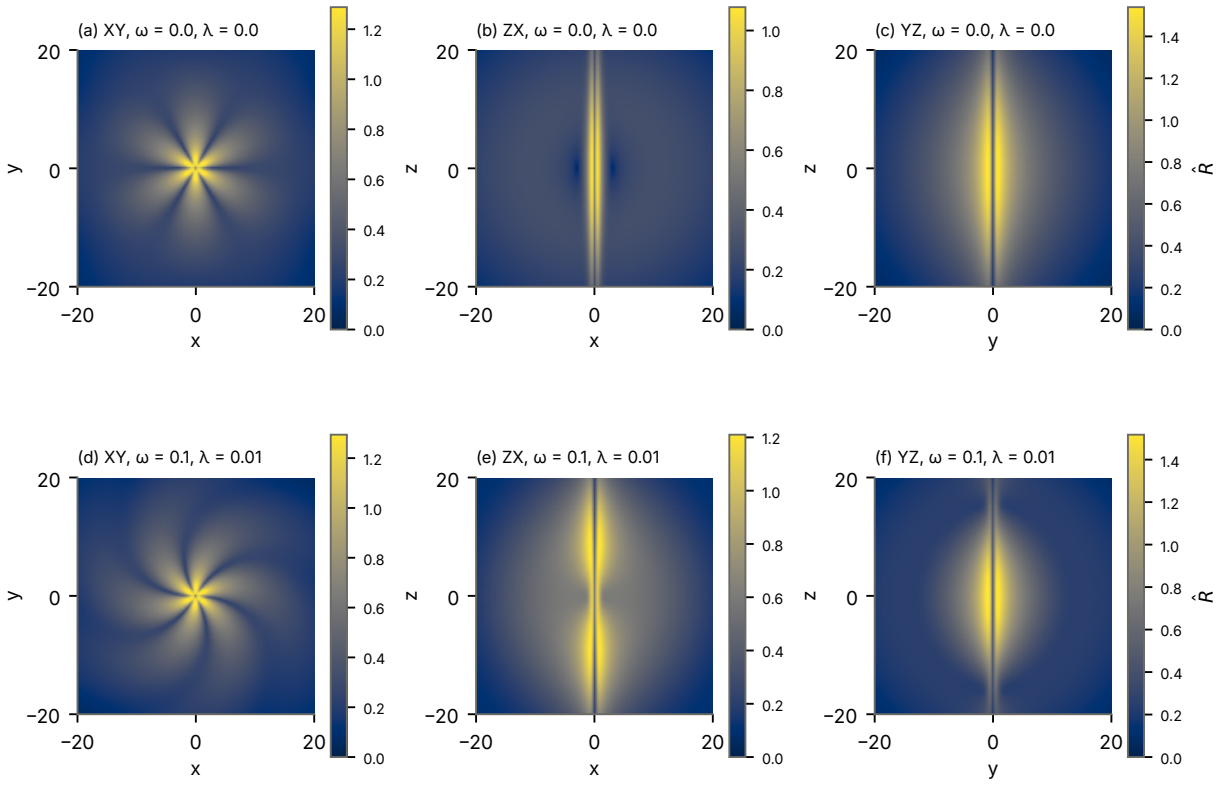


Figure 3. Normalised certainty ratio $\hat{R}$ of the regularised model ($m = 3$, $a = 0.5$, $L = 20$, $N = 257$) in the XY ($z = 0$), ZX ($y = 0$) and YZ ($x = 0$) planes. (a)-(c) No twist ($\omega = \lambda_{\mathrm{vert}} = 0$); (d)-(f) baseline twist ($\omega = 0.1$, $\lambda_{\mathrm{vert}} = 0.01$). Each panel has its own colour scale.

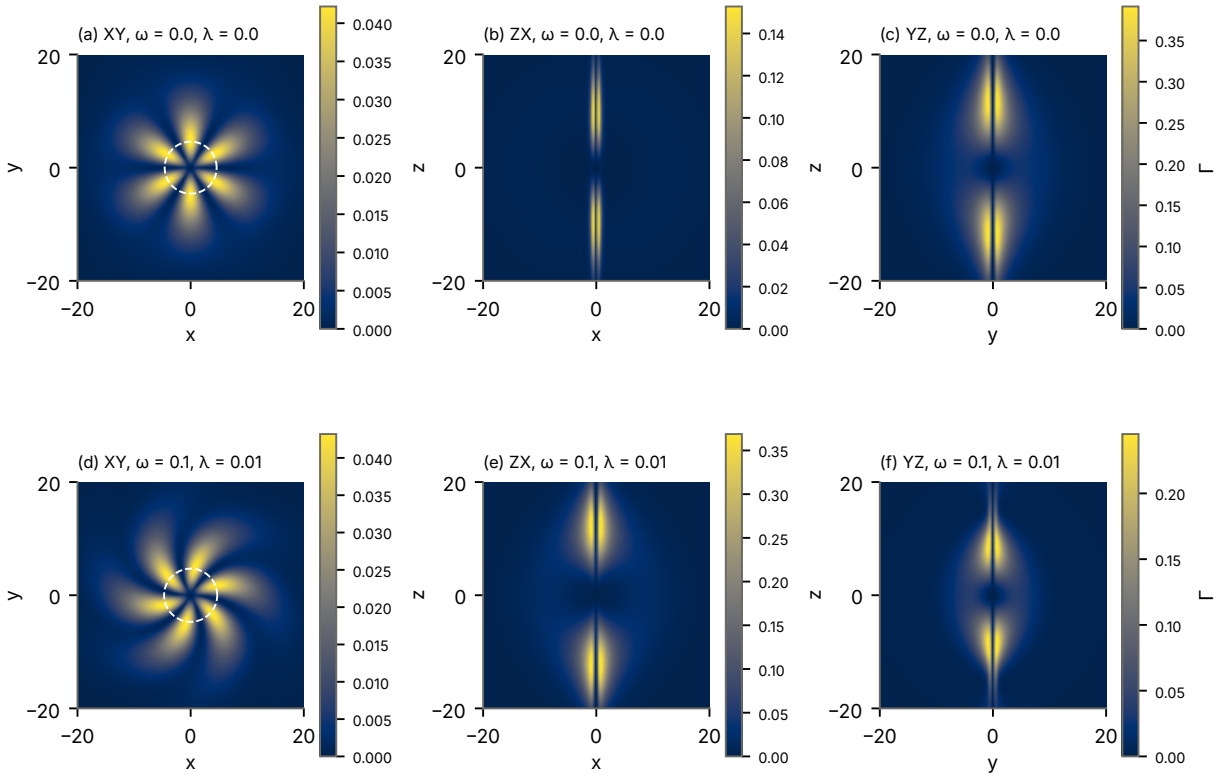


Figure 4. Decoherence field Γ for the same parameters and planes as Figure 3. The dashed circle in (a) and (d) marks the ring of largest azimuthal mean, $r^* = 4.6$ and 4.7. Each panel has its own colour scale.

the azimuthal gradient vanishes (Figure 3(a)); the radial twist bends the spokes into trailing spirals (Figure 3(d)), as Eq. (15) requires. In the meridional planes $\hat{R}$ forms a column along the symmetry axis with a dark core of radius $\sim a$, where the regularised field vanishes. Its width depends on the orientation of the plane: without twist the half-maximum half-width at $z = 0$ is 1.25 in the ZX plane but 5.5 in the YZ plane (Figure 3(b, c)). The reason is geometric: for $m = 3$ the plane $y = 0$ ($\theta = 0, \pi$) lies on a node of $\sin 3\theta$ and the plane $x = 0$ ($\theta = \pm\pi/2$) on an antinode, so the azimuthal gradient vanishes in one and is maximal in the other. This orientation dependence is what produced the narrow ("notch") and broad ("D-shaped") outlines in earlier versions of the model, which resemble the shadows of spinning black holes [33–35] only in shape. With twist, the phase ωR moves the node off the $y = 0$ plane, the ZX column broadens to a half-width of 5.8 and splits into two lobes centred at $|z| \approx 8$ (Figure 3(e)).

The decoherence field shows the same symmetry (Figure 4). In the equatorial plane it forms six spiral lobes outside an ordered core, with the largest azimuthal mean at $r^* = 4.6$ (no twist) and 4.7 (twist). In the meridional planes Γ is concentrated in two lobes on either side of the core at $|z| \approx$ 9-12, with half-widths of 0.8-2.2, and is small near the equator; this is qualitatively similar to shocks that form near the base of radiatively driven jets [36]. The semantic temperature follows $|\nabla\sigma|$ and spans $T^*/T_0 = 1$ to $1 + \beta_T = 1.1$; the semantic flux $\mathbf{j}_{\rm sem} = -k_{\rm sem}\nabla T^*$ points away from the hot spiral arms (Figure 5).

5.3 Symmetry Inheritance: Hot-Spot Multiplicity

To test whether the equatorial maxima reflect the model's dynamics or its input, I varied the azimuthal order from $m = 1$ to 6 at fixed $\omega = 0.1$, $\lambda_{\rm vert} = 0.01$. In every case Γ and $\hat{R}$ have exactly $2m$ maxima on the ring, and the dominant Fourier harmonic of the azimuthal profile is $2m$, both with and without regularisation (Figure 6). The six hot-spot-like features of the baseline model therefore follow from the choice $m = 3$. The ring radius depends on m (between $r^* = 4.1$ and 6.0 for $m =$ 1-6 at $a = 0.5$) and on the envelope width ($r^* = 3.7$, 4.7 and 5.6 for $w = 10$, 15 and 20), but not on the domain size ($L = 8$, 10 and 12 give identical r^*). A ring of $2m$ maxima is not an independent result of the model; it is a direct readout of the imposed orientation reference, which makes m measurable in principle (Section 6.3).

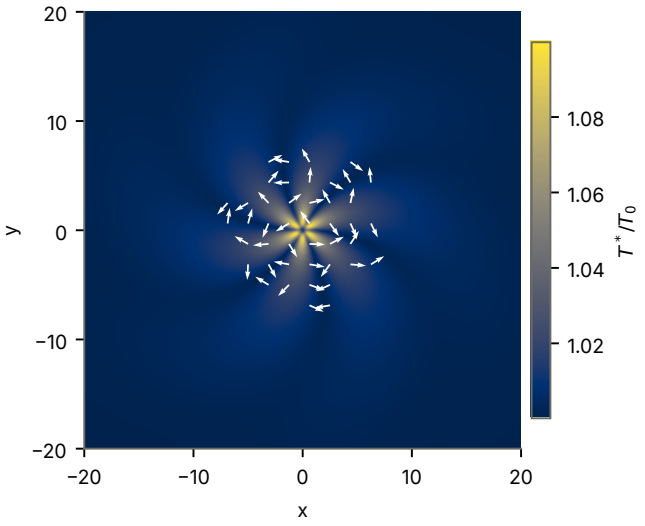


Figure 5. Semantic temperature T^*/T_0 in the equatorial plane ($\omega = 0.1$, $\lambda_{\rm vert} = 0.01$, $a = 0.5$). Arrows give the direction of the semantic flux $\mathbf{j}_{\rm sem} = -k_{\rm sem}\nabla T^*$ where its magnitude exceeds 2% of the maximum.

5.4 Closed-Form Relations: Spiral Pitch and Hemispheric Twist

Where the azimuthal gradient dominates, $|\nabla\sigma|^2 \propto \sin^2 \Phi_{\rm geo}$ on a sphere of fixed R and polar angle ϕ, so the maxima lie at $\Phi_{\rm geo} = \pi/2 + k\pi$ (Appendix D):

$$\theta_k(R, \phi) = \frac{(k + \frac{1}{2})\pi - \omega R - \lambda_{\rm vert}\cos\phi}{m}, \; k = 0, \ldots, 2m-1. \tag{14}$$

Two observable consequences follow. In the equatorial plane the maxima trace trailing spirals with pitch

$$\frac{d\theta_k}{dR} = -\frac{\omega}{m}, \tag{15}$$

and, at cylindrical radius ϱ and heights $\pm z$, the northern pattern is rotated relative to the southern one by

$$\Delta\theta_{\rm N-S} = -\frac{2\lambda_{\rm vert}}{m}\frac{z}{\sqrt{\varrho^2 + z^2}}. \tag{16}$$

Equation (16) is the chirality introduced by the $\mathbb{Z}_2$ term: stacked along z, the maxima form a helix whose handedness is the sign of $\lambda_{\rm vert}$. Both relations agree with the simulations (Figure 7). The measured pitch is -0.036, -0.173 and -0.304 for $\omega = 0.1$, 0.5 and 0.9, against predictions of -0.033, -0.167 and -0.300; the residual (9% at $\omega = 0.1$, 1.4% at $\omega = 0.9$) comes from the radial gradient terms neglected in Eq. (14). The twist at $\varrho = 4.7$, $z = \pm 3$ agrees with Eq. (16) to within 0.3% for $\lambda_{\rm vert}$ from 0.25 to 1.

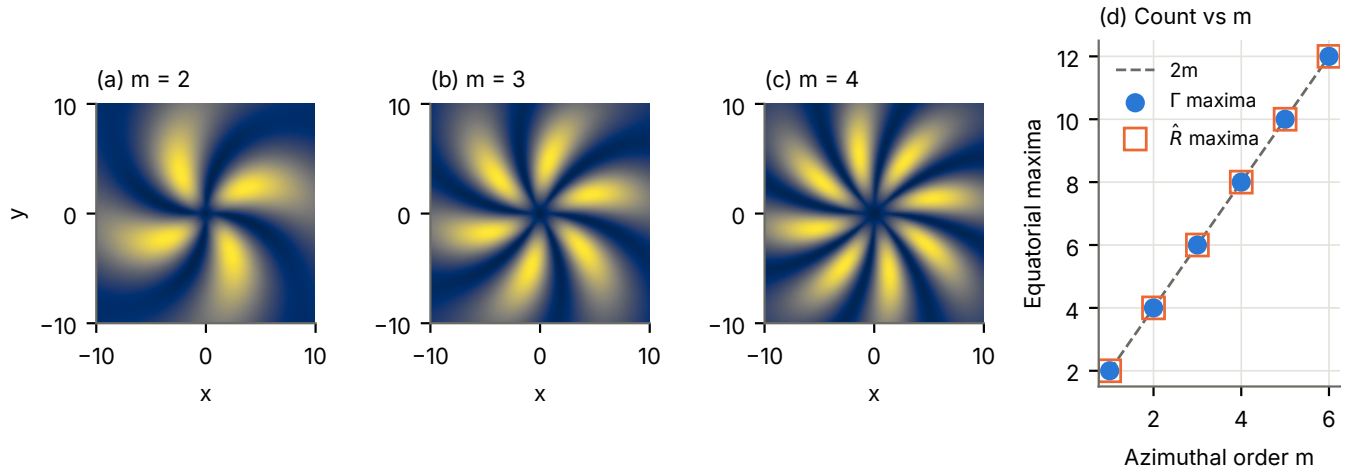


Figure 6. Control runs with azimuthal order m. (a)-(c) Decoherence field Γ in the equatorial plane for $m = 2, 3$ and 4 ($\omega = 0.1$, $\lambda_{\text{vert}} = 0.01$, $a = 0.5$, $N = 128$). (d) Number of maxima of Γ and of $\hat{R}$ on the ring of largest mean Γ; the dashed line is $2m$.

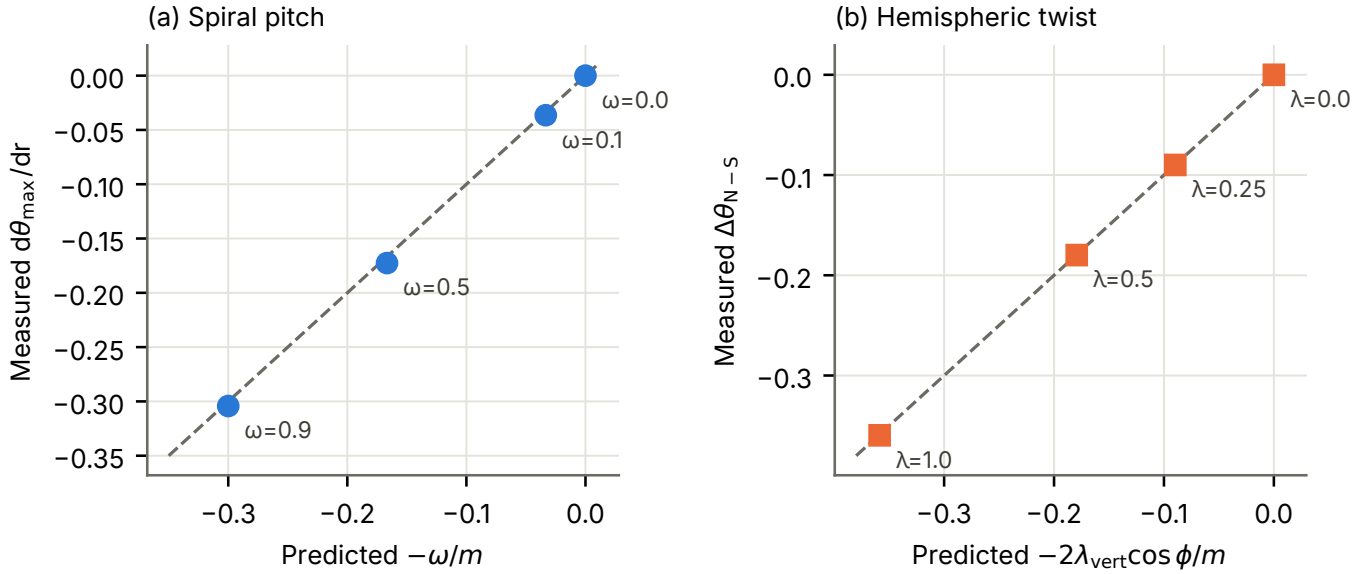


Figure 7. Closed-form relations versus simulation ($m = 3$, $a = 0.5$, $N = 160$). (a) Radial drift of the azimuth of the Γ maxima in the equatorial plane against Eq. (15). (b) Rotation of the northern ($z = 3$) relative to the southern ($z = -3$) pattern at $\varrho = 4.7$ against Eq. (16). Dashed lines mark equality.

5.5 Semantic Velocities

Table 5 lists semantic velocities from the original model for $\omega = 0.9$ and $\lambda_{\text{vert}} = 5$. Mean speeds stay between $0.31c$ and $0.36c$ at all radii, while the maximum rises from $0.66c$ near the centre to $0.78c$ at $r \approx 5.3$-6.3, with a dip to $0.44c$ at $r = 1.87$. The velocity scale is set by the fitted k_{sem}, so agreement with relativistic jet speeds [37, 38] is a calibration, not a prediction. The velocities were computed from $\mathbf{j}_{\text{sem}}$, with $a = 0$; because T^* is normalised by $|\nabla\sigma|_{\max}$, they should be recomputed with a regularised field before publication.

6 Discussion

6.1 What the Model Shows

The tests separate three classes of features. The equatorial ring of $2m$ maxima, its spiral pitch and its hemispheric twist are converged and follow closed-form relations; they are mappings from the imposed symmetry parameters to observables, not emergent dynamics. The axial, jet-like enhancement of R and Γ is anchored to the phase-defect line and is controlled by the core radius a. The velocity scale is a calibration through k_{sem}. The narrow and broad meridional outlines are a slice-orientation effect

Table 5. Semantic velocity versus radial distance r (code units) for $\omega = 0.9$, $\lambda_{\text{vert}} = 5$, $a = 0$. Columns: radius; mean and maximum speed in $10^7\,\text{m}\,\text{s}^{-1}$; maximum speed as a fraction of $c = 3.00 \times 10^8\,\text{m}\,\text{s}^{-1}$; number of grid points N_r in the bin.

r	Mean $\lvert v\rvert$ ($10^7\,\text{m}\,\text{s}^{-1}$)	Max $\lvert v\rvert$ ($10^7\,\text{m}\,\text{s}^{-1}$)	Max/c	N_r
0.50	10.16	19.89	0.663	8
0.84	10.16	19.89	0.663	8
1.18	10.16	19.89	0.663	8
1.53	9.769	19.89	0.663	32
1.87	9.638	13.13	0.438	24
2.21	10.00	17.60	0.587	48
2.55	9.643	17.60	0.587	80
2.89	9.645	17.60	0.587	56
3.24	9.666	21.43	0.714	104
3.58	9.317	21.43	0.714	104
3.92	9.691	22.93	0.764	120
4.26	9.976	22.93	0.764	192
4.61	10.09	22.93	0.764	224
4.95	10.34	22.93	0.764	272
5.29	10.71	23.31	0.777	272
5.63	10.31	23.31	0.777	272
5.97	10.09	23.31	0.777	368
6.32	9.790	23.31	0.777	408
6.66	9.577	22.75	0.758	432
7.00	9.607	22.75	0.758	512

of the m-fold pattern (Section 5.2). In real black holes, notch-shaped and D-shaped shadows arise from photon orbits in the Kerr metric [34, 35], which the model does not contain, so any resemblance is morphological only.

6.2 Comparison with Observations

The model has one free length unit. Near-infrared flares of Sgr A* are consistent with a hot spot on a near-circular orbit at about 6-10 gravitational radii r_g with a period of 45 ± 15 min [39]. Identifying the converged ring radius $r^* = 4.7$ ($w = 15$, $a = 0.5$) with this orbit fixes one code unit at 1.3-2.1 r_g. The regularisation radius $a = 0.5$ then corresponds to 0.6-1.1 r_g, comparable to the horizon scale, which suggests identifying the defect core with the horizon; this identification is a hypothesis to be tested, not a result. In M87 the inner jet shows superluminal knots [40], complex internal motions [41, 42], three helical threads [43] and a large-scale ordered helical magnetic field in the acceleration-collimation zone [44]. The model's helices (Eq. (16)) are of the right kind, and the observed handedness of the M87 field [44] would fix the sign of λ_{vert}. Nested photon subrings converge exponentially toward a critical curve set by mass and spin [45, 46]; reproducing that structure would require ray tracing, which is beyond the present model.

6.3 Falsifiable Predictions

The closed-form relations lead to predictions that observations could contradict.

1. **Flux quasi-periodicity.** If the $2m$ maxima co-rotate with the flaring gas, the integrated flux is modulated at $2m$ times the orbital frequency. For $m = 3$ and the 45 min period of Sgr A* flares [39], this predicts a sub-period near 7.5 ± 2.5 min; the absence of power at the sixth harmonic in well-sampled light curves would rule out $m = 3$.

2. **Pitch-twist relation.** Spiral features in the equatorial plane and helical features along the axis share the same m (Eqs. (15) and (16)). Measured pitch and twist angles must therefore give a consistent m.

3. **Chirality.** The handedness of jet helices should be the same at all heights above one hemisphere and reversed in the counter-jet.

4. **Mass scaling.** Thermodynamic coherence scales as $C_T = 2/(Mc^2)$, so any observable tied to C_T should scale as $1/M$ across the black-hole mass range.

6.4 Limitations

The postulates are phenomenological, and the semantic quantities have not yet been linked to measurable thermodynamic quantities by an independent calibration. The correspondence between ω, λ_{vert}, m and the reference-frame resources of Gour and Spekkens [18] is structural; no proof is given that these parameters form a complete set of frames or that R is a resource monotone. The model is static and contains no spacetime geometry, so it says nothing about rotation of the hot spots or about photon orbits. The impulse scale $\mathcal{I}_0$ and conductivity k_{sem} are free parameters, and the core radius a controls the strength of the axial features.

6.5 Outlook

Two extensions follow naturally. Mode 3 suggests treating the holographic interface as a flux of coherence through a screen, in the spirit of entropic gravity [47]; and the Mode 2 picture of black holes as processors is compatible with the cosmological coupling of black-hole masses to dark energy reported recently [48,

49]. Both require a dynamical, relativistic version of the model. The semantic heat capacity derived in Appendix C, which rises as $(T^* - T_0)^{1/2}$, may also be compared with the shape-induced specific-heat features of confined Bose gases [9, 10].

7 Conclusions

This paper formulated Coherence Thermodynamics as a phenomenological framework built on a minimum-action postulate, a gradient-based semantic entropy and an equipartition-based semantic temperature, and applied it to black holes, for which $C_T = 2/(Mc^2)$. Convergence tests showed that the original field model contains a phase-defect line on its symmetry axis, which makes the axial, jet-like structures resolution-dependent; a core regularisation restores convergence and exposes the core radius as the parameter that sets their strength. Control runs showed that the decoherence maxima number exactly $2m$, and closed-form relations for their spiral pitch and hemispheric twist agree with simulations to within 9% and 0.3%. The model therefore acts as a quantitative map from symmetry parameters to morphology, and that map yields falsifiable predictions, most directly a flux quasi-periodicity at $2m$ times the hot-spot orbital frequency. Testing these predictions, and deriving the free parameters k_{sem}, $\mathcal{I}_0$ and a from first principles, are the main tasks ahead.

Data Availability Statement

The original model notebooks are available in the *CT Code Colab* (https://colab.research.google.com/drive/1AlieY7UMf-uvvKQNIkJ8ehilDOlPUOnU) and the *Reasoning Model Colab* (https://colab.research.google.com/drive/1Np44wK3UDEV9acY698mpZ2AjZnZGuwCK). Scripts and data for Figures 2-7 are available via the CT Code Colab link above.

Funding

This work was supported without any funding.

Conflicts of Interest

The author declares no conflicts of interest.

AI Use Statement

Generative AI tools were used for coding assistance, English editing and LaTeX formatting. OpenAI ChatGPT-4o was consulted during early-stage exploration in March 2025; the certainty equation and all core theoretical contributions were independently developed by the author. Claude Sonnet 4 was used in June 2025 to help write the starter code for the CT model, which the author then substantially refined. Gemini 2.0 Flash was used for general coding assistance and English editing.

Ethical Approval and Consent to Participate

Not applicable. This study did not involve human participants or animals.

Abbreviations

C-I	Coherence-information (system)
CT	Coherence Thermodynamics
EIEO	Existential In, Existential Out
RMS	Root mean square
SSR	Superselection rule

References

[1] Landauer, R. (1961). Irreversibility and heat generation in the computing process. *IBM Journal of Research and Development*, *5*(3), 183-191. [CrossRef]

[2] Scully, M. O., Zubairy, M. S., Agarwal, G. S., & Walther, H. (2003). Extracting work from a single heat bath via vanishing quantum coherence. *Science*, *299*(5608), 862-864. [CrossRef]

[3] Scully, M. O., Chapin, K. R., Dorfman, K. E., Kim, M. B., & Svidzinsky, A. (2011). Quantum heat engine power can be increased by noise-induced coherence. *Proceedings of the National Academy of Sciences*, *108*(37), 15097-15100. [CrossRef]

[4] Baumgratz, T., Cramer, M., & Plenio, M. B. (2014). Quantifying coherence. *Physical Review Letters*, *113*(14), 140401. [CrossRef]

[5] Lostaglio, M., Jennings, D., & Rudolph, T. (2015). Description of quantum coherence in thermodynamic processes requires constraints beyond free energy. *Nature Communications*, *6*(1), 6383. [CrossRef]

[6] Faist, P., Oppenheim, J., & Renner, R. (2015). Gibbs-preserving maps outperform thermal operations in the quantum regime. *New Journal of Physics*, *17*(4), 043003. [CrossRef]

[7] Tajima, H., & Takagi, R. (2025). Gibbs-preserving operations requiring infinite amount of quantum coherence. *Physical Review Letters*, *134*(17), 170201. [CrossRef]

[8] Narasimhachar, V., & Gour, G. (2015). Low-temperature thermodynamics with quantum coherence. *Nature communications*, *6*(1), 7689. [CrossRef]

[9] Kurt, C., Sisman, A., & Aydin, A. (2025).

Shape-controlled Bose–Einstein condensation. *Physica Scripta, 100*(1), 015289. [CrossRef]

[10] Aydin, A. (2025). Geometry-induced asymmetric level coupling. *Physical Review E, 112*(1), 014121. [CrossRef]

[11] Wheeler, J. A. (2018). Information, physics, quantum: The search for links. *Feynman and computation*, 309-336.

[12] Schrodinger, E. (1944). *What Is Life? The Physical Aspect of the Living Cell*. Cambridge: Cambridge University Press. https://archive.org/details/whatislifephysic0000schr_y5x8

[13] Bekenstein, J. D. (1973). Black holes and entropy. *Physical Review D, 7*(8), 2333-2346. [CrossRef]

[14] Hawking, S. W. (1974). Black hole explosions? *Nature, 248*(5443), 30-31. [CrossRef]

[15] Dirac, P. A. M. (1930). *The Principles of Quantum Mechanics* (1st ed.). Oxford: Clarendon Press. https://archive.org/details/dli.ernet.212159

[16] Heisenberg, W. (1927). Über den anschaulichen Inhalt der quantentheoretischen Kinematik und Mechanik. *Zeitschrift für Physik, 43*(3), 172-198. [CrossRef]

[17] Shannon, C. E. (1948). A mathematical theory of communication. *The Bell system technical journal, 27*(3), 379-423. [CrossRef]

[18] Gour, G., & Spekkens, R. W. (2008). The resource theory of quantum reference frames: Manipulations and monotones. *New Journal of Physics, 10*(3), 033023. [CrossRef]

[19] Mehrabpour, H., Giacalone, G., & Luzum, M. W. (2026). Triaxial shapes and the angular structure of nuclear three-body correlations. *arXiv preprint arXiv:2604.00619*. [CrossRef]

[20] Boltzmann, L. (2012). Über die Beziehung zwischen dem zweiten Hauptsatze der mechanischen Wärmetheorie und der Wahrscheinlichkeitsrechnung resp. den Sätzen über das Wärmegleichgewicht. In F. Hasenöhrl (Ed.), *Wissenschaftliche Abhandlungen* (pp. 164–223). Cambridge University Press. [CrossRef]

[21] von Neumann, J. (1932). *Mathematische Grundlagen der Quantenmechanik*. Berlin: Springer. (English translation: *Mathematical Foundations of Quantum Mechanics*, Princeton University Press, 1955.) https://archive.org/details/mathematischegru0000vonn/page/n1/mode/2up

[22] Maxwell, J. C. (1871). *Theory of Heat*. London: Longmans, Green, and Co. https://archive.org/details/B-001-003-070

[23] Gibbs, J. W. (1875-1878). On the equilibrium of heterogeneous substances. *Transactions of the Connecticut Academy of Arts and Sciences, 3*(96), 108-248; 343-524. [CrossRef]

[24] Clausius, R. (1851). I. on the moving force of heat, and the laws regarding the nature of heat itself which are deducible therefrom. *The London, Edinburgh, and Dublin Philosophical Magazine and Journal of Science, 2*(8), 1-21. [CrossRef]

[25] Carnot, S. (1872). Réflexions sur la puissance motrice du feu et sur les machines propres à développer cette puissance. In *Annales scientifiques de l'École normale supérieure* (Vol. 1, pp. 393-457). https://www.numdam.org/item/10.24033/asens.88.pdf

[26] Nernst, W. (1906). Ueber die Berechnung chemischer Gleichgewichte aus thermischen Messungen. *Nachrichten von der Gesellschaft der Wissenschaften zu Göttingen, Mathematisch-Physikalische Klasse, 1906*, 1-40. http://dml.mathdoc.fr/item/GDZPPN002500655

[27] Nernst, W. (1918). *Die theoretischen und experimentellen Grundlagen des neuen Wärmesatzes*. Halle: Wilhelm Knapp. https://onebid.de/de/ksiazki-i-starodruki-nernst-w-die-theoretischen-und-experimentellen-grundlagen-des-neuren-warmesatzes-halle-1918/3556293

[28] Planck, M. (1911). *Vorlesungen über thermodynamik* (3rd ed.). Leipzig: Veit & Comp. [CrossRef]

[29] Vopson, M. M. (2019). The mass-energy-information equivalence principle. *AIP Advances, 9*(9), 095206. [CrossRef]

[30] Einstein, A. (1905). Ist die Trägheit eines Körpers von seinem Energieinhalt abhängig? *Annalen der Physik, 323*(13), 639-641. [CrossRef]

[31] Nye, J. F., & Berry, M. V. (1974). Dislocations in wave trains. In *A Half-Century of Physical Asymptotics and Other Diversions: Selected Works by Michael Berry* (pp. 6-31). [CrossRef]

[32] LeVeque, R. J. (2007). *Finite Difference Methods for Ordinary and Partial Differential Equations: Steady-State and Time-Dependent Problems*. Philadelphia: SIAM. [CrossRef]

[33] James, O., von Tunzelmann, E., Franklin, P., & Thorne, K. S. (2015). Gravitational lensing by spinning black holes in astrophysics, and in the movie *Interstellar*. *Classical and Quantum Gravity, 32*(6), 065001. [CrossRef]

[34] Bardeen, J. M. (1973). Timelike and null geodesics in the Kerr metric. *Black holes* (*Les astres occlus*), 215-239. https://inis.iaea.org/records/g26q5-w9k04

[35] Hioki, K., & Maeda, K. (2009). Measurement of the Kerr spin parameter by observation of a compact object's shadow. *Physical Review D, 80*(2), 024042. [CrossRef]

[36] Joshi, R. K., Debnath, S., & Chattopadhyay, I. (2022). Shocks in radiatively driven time-dependent, relativistic jets around black holes. *The Astrophysical Journal, 933*(1), 75. [CrossRef]

[37] Blandford, R. D., & Znajek, R. L. (1977). Electromagnetic extraction of energy from Kerr black holes. *Monthly Notices of the Royal Astronomical Society, 179*(3), 433-456. [CrossRef]

[38] Mertens, F., Lobanov, A. P., Walker, R. C., & Hardee, P. E. (2016). Kinematics of the jet in M 87 on scales of 100–1000 Schwarzschild radii. *Astronomy & Astrophysics, 595*, A54. [CrossRef]

[39] GRAVITY Collaboration, Abuter, R., Amorim, A., Baubock, M., Berger, J. P., Bonnet, H., ... & Yazici, S. (2018). Detection of orbital motions near the last stable circular orbit of the massive black hole SgrA. *Astronomy & Astrophysics, 618*, L10. [CrossRef]

[40] Biretta, J. A., Sparks, W. B., & Macchetto, F. (1999). Hubble Space Telescope observations of superluminal motion in the M87 jet. *The Astrophysical Journal, 520*(2), 621. [CrossRef]

[41] Walker, R. C., Hardee, P. E., Davies, F. B., Ly, C., & Junor, W. (2018). The structure and dynamics of the subparsec jet in M87 based on 50 VLBA observations over 17 years at 43 GHz. *The Astrophysical Journal, 855*(2), 128. [CrossRef]

[42] Nakamura, M., Asada, K., Hada, K., Pu, H. Y., Noble, S., Tseng, C., ... & Tazaki, F. (2018). Parabolic jets from the spinning black hole in M87. *The Astrophysical Journal, 868*(2), 146. [CrossRef]

[43] Nikonov, A. S., Kovalev, Y. Y., Kravchenko, E. V., Pashchenko, I. N., & Lobanov, A. P. (2023). Properties of the jet in M87 revealed by its helical structure imaged with the VLBA at 8 and 15 GHz. *Monthly Notices of the Royal Astronomical Society, 526*(4), 5949-5963. [CrossRef]

[44] Park, J., Takahashi, K., Toma, K., Hada, K., Nakamura, M., Pu, H. Y., ... & Cho, I. (2026). Helical magnetic field in the acceleration-collimation zone of the M87 jet. *The Astrophysical Journal Letters, 996*(2), L22. [CrossRef]

[45] Vincent, F. H., Gralla, S. E., Lupsasca, A., & Wielgus, M. (2022). Images and photon ring signatures of thick disks around black holes. *Astronomy & Astrophysics, 667*, A170. [CrossRef]

[46] Johnson, M. D., Lupsasca, A., Strominger, A., Wong, G. N., Hadar, S., Kapec, D., ... & Moran, J. M. (2020). Universal interferometric signatures of a black hole's photon ring. *Science advances, 6*(12), eaaz1310. [CrossRef]

[47] Verlinde, E. (2011). On the origin of gravity and the laws of Newton. *Journal of High Energy Physics*, 2011(4), 029. [CrossRef]

[48] Farrah, D., Croker, K. S., Zevin, M., Tarlé, G., Faraoni, V., Petty, S., ... & Weiner, J. (2023). Observational evidence for cosmological coupling of black holes and its implications for an astrophysical source of dark energy. *The Astrophysical Journal Letters, 944*(2), L31. [CrossRef]

[49] Croker, K. S., Tarlé, G., Ahlen, S. P., Cartwright, B. G., Farrah, D., Fernandez, N., & Windhorst, R. A. (2024). DESI dark energy time evolution is recovered by cosmologically coupled black holes. *Journal of Cosmology and Astroparticle Physics, 2024*(10), 094. [CrossRef]

Jordan Barton is an independent researcher. His research interests include information thermodynamics, quantum coherence and black-hole astrophysics. (Email: jbiophysics@gmail.com)

Appendix

A Units of the Semantic Temperature

The phase ϕ is dimensionless, so $(\partial_0\phi)^2$ has units of s^{-2}. The semantic kinetic parameter κ_Ψ [$\mathrm{J\,s^2\,m^{-3}}$] turns it into an energy density, and multiplying by the volume V_Ψ and dividing by Nk_B gives kelvin (Table A1).

Table A1. Units of the quantities in Eq. (4).

Symbol	Quantity	Units
κ_Ψ	Semantic kinetic parameter	$\mathrm{J\,s^2\,m^{-3}}$
V_Ψ	Semantic volume	$\mathrm{m^3}$
$\langle(\partial_0\phi)^2\rangle$	Mean-square phase rate	$\mathrm{s^{-2}}$
N	Processing elements	1
k_B	Boltzmann constant	$\mathrm{J\,K^{-1}}$
T^*	Semantic temperature	K

B Derivations of the Laws

B.1 Zeroth Law

Operationally T^* is proportional to the rate of resolved contradictions, $T^* \propto \lim_{\Delta t\to 0}\Delta N_{\mathrm{contr}}/\Delta t$; in field terms $T^* \propto \langle(\partial_0\phi)^2\rangle$, and at equilibrium the two measures coincide. Semantic heat flows down the temperature difference, $Q^*_{A\to B} \propto T^*_A - T^*_B$, so equilibrium (no net flow) requires $T^*_A = T^*_B$. If $T^*_A = T^*_C$ and $T^*_B = T^*_C$, transitivity gives $T^*_A = T^*_B$.

B.2 First Law

The semantic internal energy changes through semantic heat, $\delta Q^{\mathrm{sem}} = T^* dS^*$, by analogy with $\delta Q_{\mathrm{rev}} = T\,dS$; through entity work, $\mu\,dN$, where μ [J per entity] is the energy needed to add one semantic unit; and through coherence work, $\Phi\,d\alpha$, where Φ [J] is the energy per unit change of the coherence scalar

$$\alpha = \frac{A_{\mathrm{coh}}}{A_{\mathrm{tot}}} \in (0, 1], \tag{A1}$$

the ratio of activity aligned with a single resolution trajectory to all semantic activity. Energy conservation gives Eq. (5). At fixed E_{sem}, a local decrease of entropy

must be paid for by $\mu\, dN > 0$ or $\Phi\, d\alpha > 0$, so local ordering cannot continue without an energy supply.

B.3 Second Law

For a volume V with entropy $S = \int_V s\, d^3x$, entropy changes by boundary flux and internal production, $dS/dt = -\oint_{\partial V} \mathbf{j}_R \cdot d\mathbf{A} + \int_V \Pi\, d^3x$. The divergence theorem and the arbitrariness of V give Eq. (6); $\Pi \geq 0$ is the second law, and $\partial s/\partial t < 0$ requires $\nabla \cdot \mathbf{j}_R > \Pi$.

B.4 Third Law

From Eq. (11), $T^* \geq T_0$, so the limit $T^* \to 0$ requires both $T_0 \to 0$ and $|\nabla\sigma| \to 0$. Then $C_S \to 1$ and $S^* \to 0$ by Eq. (3).

B.5 Fourth Law

The minimum energy per resolved bit is $k_B T^* \ln 2$; dividing by c^2 gives the mass per bit, and multiplying by ρ_I gives Eq. (7) in $\mathrm{kg\,m^{-3}}$. A volume whose information moves with velocity $\mathbf{v}$ then resists acceleration with $\mathbf{F} = \int_V \rho\, (D\mathbf{v}/Dt)\, dV$ [N].

C Semantic Heat Capacity

With $C^* = dE_{\mathrm{sem}}/dT^*$ and $dN = d\alpha = 0$, $C^* = T^* dS^*/dT^*$. Inverting Eq. (11), $|\nabla\sigma| = (|\nabla\sigma|_{\max}/\beta_T)(T^*/T_0 - 1)$, and Eq. (3) gives

$$S^* = \alpha k_B \left[\frac{r_G}{\beta_T}\left(\frac{T^*}{T_0} - 1\right)\right]^{3/2}, \qquad r_G = \frac{|\nabla\sigma|_{\max}}{G_0}, \tag{A2}$$

so that

$$C^* = \frac{3}{2}\alpha k_B \left(\frac{r_G}{\beta_T}\right)^{3/2} \frac{T^*}{T_0}\left(\frac{T^*}{T_0} - 1\right)^{1/2}, \qquad T^* \geq T_0. \tag{A3}$$

C^* vanishes at $T^* = T_0$ and has no divergence. With $a = 0$, r_G grows with resolution (Section 5.1), so a regularised field is needed for a finite C^*.

D Closed-Form Relations for the Maxima

Write $\Phi \equiv \Phi_{\mathrm{geo}}$ and consider $\varrho \gg a$ so that $f_a \approx 1$. The gradient of $\sigma = g\cos\Phi$ has a radial part $g'\cos\Phi - g\omega\sin\Phi$, an azimuthal part $-gm\sin\Phi/\varrho$ and a polar part $g\lambda_{\mathrm{vert}}\sin\phi\sin\Phi/R$. Where the azimuthal part dominates, i.e. $m/\varrho \gg |g'/g|, \omega$,

$$|\nabla\sigma|^2 \simeq g^2\left[\frac{m^2}{\varrho^2} + \frac{\lambda_{\mathrm{vert}}^2 \sin^2\phi}{R^2}\right]\sin^2\Phi, \tag{A4}$$

which at fixed (R, ϕ) is maximal at $\Phi = (k + \frac{1}{2})\pi$. Since Φ increases by $2m\pi$ as θ goes once around, there are exactly $2m$ maxima, at the azimuths of Eq. (14). Because Γ and $\hat{R}$ increase monotonically with $|\nabla\sigma|$ at fixed position, they have the same maxima. Differentiating Eq. (14) at fixed $\phi = \pi/2$ gives Eq. (15); evaluating it at $\cos\phi = \pm z/R$ and subtracting gives Eq. (16). The neglected radial term shifts the maxima slightly toward the zeros of $\cos\Phi$; its relative weight $\omega\varrho/m$ explains the 9% residual in the pitch at small ω, where the shift is comparable to the drift being measured.